Application of DInSAR-GPS Optimization for Derivation of Fine-Scale Surface Motion Maps of Southern California

Sergey Samsonov, Kristy Tiampo, John Rundle, and Zhenhong Li

***Abstract*—A method based on random field theory and Gibbs–Markov random fields equivalency within Bayesian statistical framework is used to derive 3-D surface motion maps from sparse global positioning system (GPS) measurements and differential interferometric synthetic aperture radar (DInSAR) interferogram in the southern California region. The minimization of the Gibbs energy function is performed analytically, which is possible in the case when neighboring pixels are considered independent. The problem is well posed and the solution is unique and stable and not biased by the continuity condition. The technique produces a 3-D field containing estimates of surface motion on the spatial scale of the DInSAR image, over a given time period, complete with error estimates. Significant improvement in the accuracy of the vertical component and moderate improvement in the accuracy of the horizontal components of velocity are achieved in comparison with the GPS data alone. The method can be expanded to account for other available data sets, such as additional interferograms, lidar, or leveling data, in order to achieve even higher accuracy.**

***Index Terms*—Bayesian statistic, differential interferometric synthetic aperture radar (DInSAR), global positioning system (GPS), Markov random field.**

I. Introduction

In OUR previous paper [1], we presented a method that allows the use of global positioning system (GPS) and differential interferometric synthetic aperture radar (DInSAR) data sets for generating 3-D high-resolution surface motion maps.

The complementary nature of these two observation techniques is apparent. The GPS measures 3-D coordinates of continuous-recording GPS sites with high temporal but low spatial resolution. The best spatial resolution currently achieved is about 25 km for the GPS Earth Observation Network in Japan [2] and 10–25 km for the Southern California Integrated GPS Network (SCIGN) in some areas of southern California [3]. DInSAR, on the other hand, measures the total deformation between two acquisition scenes projected in the line of sight (LOS) (direction between satellite and point on the ground) with high spatial resolution over a wide area, but low temporal resolution. The best temporal resolution of 35 days suitable for long-term continuous measurements was achieved by European Remote Sensing 1 and 2 (ERS-1/2) satellite missions between 1992–2005, when not considering tandem pairs with temporal resolution of one day between 1995–2000 which are not suitable for long-term deformation studies but very useful for coseismic measurements [4].

In [1], we showed that if each point of the surface is considered independent of its neighborhood, than the method proposed in [5] can be significantly simplified and a unique and stable solution can be calculated analytically without appealing to computationally expensive minimization techniques such as Monte Carlo simulated annealing method.

Nevertheless, it is important to understand that the condition of independence does not actually imply that the neighboring points on the ground are independent. This condition simply means that that part of the information which potentially could be derived from their dependence is not considered in this model. However, with this assumption, DInSAR and GPS data can be joined together in a unique way, which is quite significant because, by itself, DInSAR data is ambiguous for the derivation of the vector velocity field.

In [1], we also presented the results of the computer simulations. There we recreated a synthetic surface motion map and showed that accuracy (expressed as rms error) drastically increases if two data sets such as GPS and DInSAR are used in lieu of the GPS data set alone, again in comparison with the original method proposed in [5].

In this paper, we apply this optimization method to data from the southern California region. The GPS and DInSAR integration approach is particularly interesting for this region. This is because the regional plate motion is inherently smooth in southern California and can be successfully measured by GPS, but in smaller fault areas it is not smooth due to local effects, which can be successfully measured by DInSAR [6], [7]. At the same time, complete understanding of the motion on both large and small scales is very important for the understanding of local seismicity.

Manuscript received January 1, 2006; revised September 15, 2006. This work was supported in part by the Natural Sciences and Engineering Research Council of Canada (NSERC) Discovery Grant and in part by the Canadian Society of Exploration Geophysicists, Canadian Exploration Geophysical Society (KEGS) Pioneers, and Society of Exploration Geophysicists scholarships received by S. Samsonov. The work of K. Tiampo was supported by an NSERC Discovery Grant. The work of J. Rundle was supported by a grant from the National Aeronautics and Space Administration under Grant NAG5-13743 to the University of California, Davis.

S. Samsonov and K. Tiampo are with the Department of Earth Sciences, University of Western Ontario, London, ON N6A 5B7, Canada (e-mail: ssamsono@uwo.ca; ktiampo@uwo.ca).

J. Rundle is with the Center for Computational Science and Engineering, University of California, Davis, CA 95616 USA (e-mail: rundle@cse.ucdavis.edu).

Z. Li is with the Department of Geomatic Engineering, University College London, WC1E 6BT London, U.K. (e-mail: zhli@ge.ucl.ac.uk).

Color versions of one or more of the figures in this paper are available online at http://ieeexplore.ieee.org.

Digital Object Identifier 10.1109/TGRS.2006.887166

Here, we show that proposed method significantly improves the accuracy of the sparse velocity measurements derived from the GPS data alone and also can be used to derive high-resolution continuous maps of the surface velocity field, complete with the corresponding horizontal and vertical errors, on both large and small scales with improved accuracy.

II. Method

Our goal is to construct continuous velocity maps of a given region, which will contain the information from two data sources continuous GPS observations and DInSAR interferograms. As it was shown in [1], the solution of this problem is found by the minimization of the energy function originally proposed in [5] with respect to its arguments. In that form, the energy function combines GPS and DInSAR data in unambiguous way and its solution can be found analytically.

The DInSAR interferogram can be related to components of the velocity vector according to the following equations:

$$\begin{aligned} V^i_{\mathrm{LOS}} &= \left[v^i_x, v^i_y, v^i_z\right] \left[S_x, S_y, S_z\right]^{\mathrm{T}} \\ &= v^i_x S_x + v^i_y S_y + v^i_z S_z \end{aligned} \tag{1}$$

where V^i_{LOS} is the known differential interferogram defined on a grid of N points, $[v^i_x, v^i_y, v^i_z]$ are unknown components of the velocity vector and $[S_x, S_y, S_z]$ are unit vectors pointing from the ground toward the satellite.

The GPS velocities, which are known only at a few sparse locations, have to be interpolated in order to create an initial continuous velocity map with similar spatial resolution as the DInSAR interferogram

$$V^i = \left[V^i_x, V^i_y, V^i_z\right]. \tag{2}$$

In this paper, we use an ordinary kriging [8], [9] interpolation technique which was suggested in [5]. However, ordinary kriging might not be always suitable and, therefore, different interpolation method must be chosen depending on the nature of the motion.

The energy function now can be rewritten in the following form, where the first term corresponds to DInSAR and the last three terms correspond to GPS:

$$\begin{aligned} u(v_x, v_y, v_z) = \sum_{i=1}^{N} \Big\{ & C^i_{\mathrm{ins}} \left(V^i_{\mathrm{LOS}} - S^i_x v^i_x - S^i_y v^i_y - S^i_z v^i_z\right)^2 \\ & + C^i_x \left(V^i_x - v^i_x\right)^2 + C^i_y \left(V^i_y - v^i_y\right)^2 + C^i_z \left(V^i_z - v^i_z\right)^2 \Big\} \end{aligned} \tag{3}$$

with coefficients

$$\begin{aligned} C^i_{\mathrm{ins}} &= \frac{1}{2(\sigma^i_{\mathrm{ins}})^2} \quad C^i_x = \frac{1}{2(\sigma^i_x)^2} \\ C^i_y &= \frac{1}{2(\sigma^i_y)^2} \quad C^i_z = \frac{1}{2(\sigma^i_z)^2} \end{aligned} \tag{4}$$

where the σ's are the standard deviations of the measurements. In this form, the (3) very closely resembles the energy function proposed in [5] but without the smoothness term.

The (3) is a function of $3 \times N$ variables $[v^i_x, v^i_y, v^i_z]$ where N is the number of grid points. It consist of N nonnegative terms corresponding to the same index i. Therefore, the function $u(v_x, v_y, v_z)$ reaches its global minimum when each subgroup with the same index i is minimal, and the first partial derivatives $(\partial u)/(\partial v^i_x)$, $(\partial u)/(\partial v^i_y)$, $(\partial u)/(\partial v^i_z)$ are equal to zero

$$\begin{aligned} \frac{\partial u}{\partial v^i_x} &= -2C^i_{\mathrm{ins}} S^i_x \left(V^i_{\mathrm{LOS}} - S^i_x v^i_x - S^i_y v^i_y - S^i_z v^i_z\right) \\ &\quad - 2C^i_x \left(V^i_x - v^i_x\right) = 0 \\ \frac{\partial u}{\partial v^i_y} &= -2C^i_{\mathrm{ins}} S^i_y \left(V^i_{\mathrm{LOS}} - S^i_x v^i_x - S^i_y v^i_y - S^i_z v^i_z\right) \\ &\quad - 2C^i_y \left(V^i_y - v^i_y\right) = 0 \\ \frac{\partial u}{\partial v^i_z} &= -2C^i_{\mathrm{ins}} S^i_z \left(V^i_{\mathrm{LOS}} - S^i_x v^i_x - S^i_y v^i_y - S^i_z v^i_z\right) \\ &\quad - 2C^i_z \left(V^i_z - v^i_z\right) = 0. \end{aligned} \tag{5}$$

This set of three linear equations with three unknowns can be constructed for each grid point. It can be rewritten in matrix form, omitting i indexes

$$\begin{vmatrix} a_{11} & a_{12} & a_{13} \\ a_{21} & a_{22} & a_{23} \\ a_{31} & a_{32} & a_{33} \end{vmatrix} \begin{vmatrix} v_x \\ v_y \\ v_z \end{vmatrix} = \begin{vmatrix} C_x V_x + S_x C_{\mathrm{ins}} V_{\mathrm{LOS}} \\ C_y V_y + S_y C_{\mathrm{ins}} V_{\mathrm{LOS}} \\ C_z V_z + S_z C_{\mathrm{ins}} V_{\mathrm{LOS}} \end{vmatrix} \tag{6}$$

where

$$\begin{aligned} a_{11} &= S^2_x C_{\mathrm{ins}} + C_x \quad a_{12} = C_{\mathrm{ins}} S_x S_y \quad a_{13} = C_{\mathrm{ins}} S_x S_z \\ a_{21} &= C_{\mathrm{ins}} S_y S_x \quad a_{22} = S^2_y C_{\mathrm{ins}} + C_y \quad a_{23} = C_{\mathrm{ins}} S_y S_z \\ a_{31} &= C_{\mathrm{ins}} S_x S_z \quad a_{32} = C_{\mathrm{ins}} S_y S_z \quad a_{33} = S^2_z C_{\mathrm{ins}} + C_z. \end{aligned} \tag{7}$$

When $\det A = |A| = C_{\mathrm{ins}} C_y C_z S^2_x + C_{\mathrm{ins}} C_x C_z S^2_y + C_{\mathrm{ins}} C_x C_y S^2_z + C_x C_y C_z$ is not equal to zero, the matrix A can be successfully inverted, and the full solution can be presented in the form

$$\begin{vmatrix} v_x \\ v_y \\ v_z \end{vmatrix} = \frac{1}{|A|} \begin{vmatrix} b_{11} & b_{12} & b_{13} \\ b_{21} & b_{22} & b_{23} \\ b_{31} & b_{32} & b_{33} \end{vmatrix} \begin{vmatrix} C_x V_x + S_x C_{\mathrm{ins}} V_{\mathrm{LOS}} \\ C_y V_y + S_y C_{\mathrm{ins}} V_{\mathrm{LOS}} \\ C_z V_z + S_z C_{\mathrm{ins}} V_{\mathrm{LOS}} \end{vmatrix} \tag{8}$$

where

$$\begin{aligned} |A| &= C_{\mathrm{ins}} C_y C_z S^2_x + C_{\mathrm{ins}} C_x C_z S^2_y + C_{\mathrm{ins}} C_x C_y S^2_z + C_x C_y C_z \\ b_{11} &= C_{\mathrm{ins}} C_z S^2_y + C_{\mathrm{ins}} C_y S^2_z + C_y C_z \\ b_{12} &= -C_{\mathrm{ins}} C_z S_x S_y \\ b_{13} &= -C_{\mathrm{ins}} C_y S_x S_z \\ b_{21} &= -C_{\mathrm{ins}} C_z S_x S_y \\ b_{22} &= C_{\mathrm{ins}} C_z S^2_x + C_{\mathrm{ins}} C_x S^2_z + C_x C_z \\ b_{23} &= -C_{\mathrm{ins}} C_x S_y S_z \\ b_{31} &= -C_{\mathrm{ins}} C_y S_x S_z \\ b_{32} &= -C_{\mathrm{ins}} C_x S_y S_z \\ b_{33} &= C_{\mathrm{ins}} C_x S^2_y + C_{\mathrm{ins}} C_y S^2_x + C_x C_y. \end{aligned} \tag{9}$$

Therefore, analytical minimization of (3) is always possible and a unique and stable solution of the optimization problem always exists, except in the particular case of $|A| = 0$.

III. Estimation of Errors of GPS–DInSAR Optimization

Here, we want to estimate the errors of the calculated (8) velocities v_x, v_y, v_z assuming that both DInSAR and GPS errors are known. According to [10], if $z = f(x, y)$ is the function of two variables x and y which are measured with the errors σ_x and σ_y, then the total error of z will be calculated by the following equation:

$$\sigma_z^2 = \left(\frac{\partial f}{\partial x}\right)^2 \sigma_x^2 + \left(\frac{\partial f}{\partial y}\right)^2 \sigma_y^2 + 2\frac{\partial f}{\partial x}\frac{\partial f}{\partial y}\sigma_{xy} \tag{10}$$

where σ_{xy} is the covariance of the pair x, y.

Often the estimation of σ_{xy} is quite complicated, however, in our case the second derivatives $(\partial f/\partial x) \cdot (\partial f/\partial y)$ are always equal to zero, and the calculation of covariance is not required.

The errors of the newly estimated velocities, therefore, can be calculated as follows:

$$\begin{aligned}
\sigma_{v_x}^2 &= \left(\frac{\partial v_x}{\partial V_{\mathrm{LOS}}}\right)^2 \sigma_{V_{\mathrm{LOS}}}^2 + \left(\frac{\partial v_x}{\partial V_x}\right)^2 \sigma_{V_x}^2 \\
&\quad + \left(\frac{\partial v_x}{\partial V_y}\right)^2 \sigma_{V_y}^2 + \left(\frac{\partial v_x}{\partial V_z}\right)^2 \sigma_{V_z}^2 \\
\sigma_{v_y}^2 &= \left(\frac{\partial v_y}{\partial V_{\mathrm{LOS}}}\right)^2 \sigma_{V_{\mathrm{LOS}}}^2 + \left(\frac{\partial v_y}{\partial V_x}\right)^2 \sigma_{V_x}^2 \\
&\quad + \left(\frac{\partial v_y}{\partial V_y}\right)^2 \sigma_{V_y}^2 + \left(\frac{\partial v_y}{\partial V_z}\right)^2 \sigma_{V_z}^2 \\
\sigma_{v_z}^2 &= \left(\frac{\partial v_z}{\partial V_{\mathrm{LOS}}}\right)^2 \sigma_{V_{\mathrm{LOS}}}^2 + \left(\frac{\partial v_z}{\partial V_x}\right)^2 \sigma_{V_x}^2 \\
&\quad + \left(\frac{\partial v_z}{\partial V_y}\right)^2 \sigma_{V_y}^2 + \left(\frac{\partial v_z}{\partial V_z}\right)^2 \sigma_{V_z}^2
\end{aligned} \tag{11}$$

where

$$\begin{aligned}
\frac{\partial v_x}{\partial V_{\mathrm{LOS}}} &= C_{\mathrm{ins}}(S_x b_{11} + S_y b_{12} + S_z b_{13}) \\
\frac{\partial v_x}{\partial V_x} &= C_x b_{11} \quad \frac{\partial v_x}{\partial V_y} = C_y b_{12} \quad \frac{\partial v_x}{\partial V_z} = C_z b_{13} \\
\frac{\partial v_y}{\partial V_{\mathrm{LOS}}} &= C_{\mathrm{ins}}(S_x b_{21} + S_y b_{22} + S_z b_{23}) \\
\frac{\partial v_y}{\partial V_x} &= C_x b_{21} \quad \frac{\partial v_y}{\partial V_y} = C_y b_{22} \quad \frac{\partial v_y}{\partial V_z} = C_z b_{23} \\
\frac{\partial v_z}{\partial V_{\mathrm{LOS}}} &= C_{\mathrm{ins}}(S_x b_{31} + S_y b_{32} + S_z b_{33}) \\
\frac{\partial v_z}{\partial V_x} &= C_x b_{31} \quad \frac{\partial v_z}{\partial V_y} = C_y b_{32} \quad \frac{\partial v_z}{\partial V_z} = C_z b_{33}.
\end{aligned} \tag{12}$$

IV. Data

Two data sets, GPS and DInSAR, are required for the derivation of high-resolution surface velocity maps. The GPS data must have sufficiently dense spatial resolution in order to estimate correctly the large-scale motion. The approximate number of the GPS stations required for this type of study must be estimated separately for each particular region of interest and will depend on it tectonic complexity.

In addition, in order to estimate velocities of the GPS sites with acceptable accuracy by applying linear regression, as in this paper, or by fitting a more complicated model, it is necessary to have sufficiently long time series. However, the long time span affects DInSAR data since interferometric measurements decorrelate quickly over time, especially in regions with strong vegetation coverage. Therefore, the optimal time span suitable for both data sets must be chosen carefully. For the regions without strong vegetation coverage the 2–3 years time span seems to be optimal; however, it can be even longer if additional interferograms, stacking, or a permanent scatters analysis method [11] is used in conjunction with this technique.

A. Region Description

We computed here 3-D surface velocity maps for that part of southern California between the Los Angeles basin and the San Gabriel mountains. The total velocity field of this region is quite complicated. It consists of the complex tectonic signal due to plate motion as well as anthropogenic signals such as those due to groundwater and oil extractions. Dense population and rapid industrial development make this area very interesting for earthquake hazard studies.

The most rapid movements in this region are nontectonic deformations due to groundwater and oil extraction. Parts of the Los Angeles basin exhibit seasonal vertical movement of up to 110 mm per year due to annual variation in the elevation of the water table [12]. The 40-km-long Santa Ana basin subsides at the steady rate of 12 mm/year with the seasonal fluctuation of 55 mm in the vertical direction and 7 mm in the horizontal direction [7]. The horizontal movement is governed mostly by plate tectonics ranging from 1.8 cm/year (south) to 0.9 cm/year (north) in the north–south direction and from -4 cm/year (southwest) to -3.2 (northeast) in the east–west direction. In [12], it was estimated that after removing anthropogenic signals the uniaxial contraction across the Los Angeles basin can be observed with the rate of 0.44 cm/year in the northeast direction perpendicular to the major strike-slip faults in this area.

B. GPS Data

In this paper, the time series from 140 GPS stations from the SCIGN were used. The data was preprocessed in order to remove outliers and offsets. Three components (north, east, and up) of the velocity vector were calculated by applying linear regression to the time series over a period corresponding to the time span of differential interferogram.

C. Kriging of the GPS Data

Sparse velocity data was interpolated by ordinary kriging [8], [9] with the help of GSTAT (program for geostatistical modeling, prediction and simulation) [13] in order to form

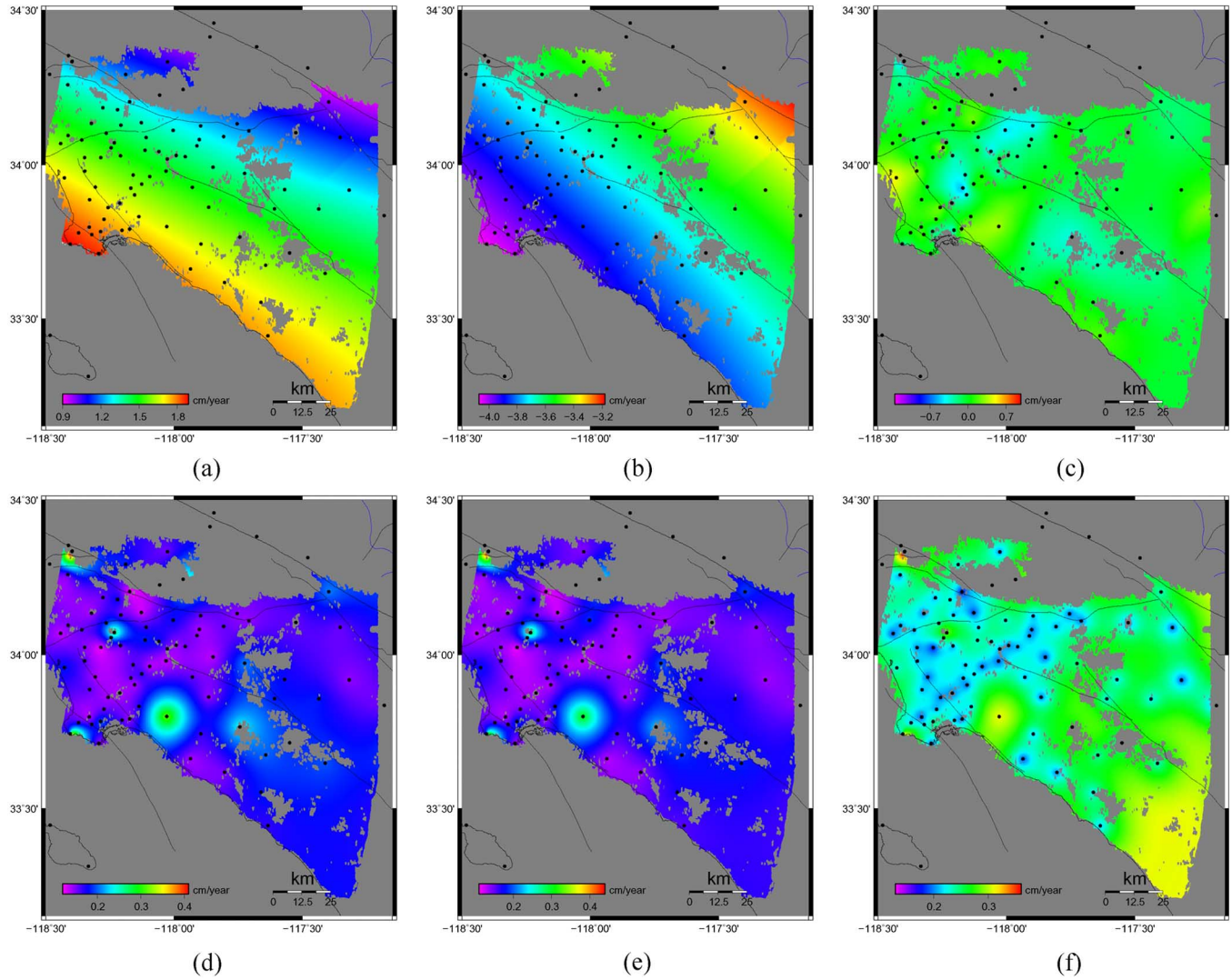

Fig. 1. Components of the surface velocity field with corresponding errors for the southern California region near Los Angeles, based on local GPS measurements from the Southern California Integrated GPS Network. The velocities of the GPS sites (black dots) were interpolated by ordinary kriging in order to form a continuous velocity map. The velocities at the GPS sites were calculate by applying linear regression to the time series. The known faults are shown as thin black lines. (a) Kriged V_{north} component of velocity. (b) Kriged V_{east} component of velocity. (c) Kriged V_{up} component of velocity. (d) Standard deviation of V_{north}. (e) Standard deviation of V_{east}. (f) Standard deviation of V_{up}.

three continuous velocity maps with the same discretization and geocoding as the DInSAR image.

Kriging is a method of interpolation, which predicts unknown values from data observed at known locations. This method uses a variogram to express the spatial variation in the data, and it minimizes the error of predicted values which are estimated by the spatial distribution of the predicted values. There are different types of kriging. However, the application of ordinary kriging for the interpolation of GPS data was suggested in [5] and works well, especially for the rough approximation of the surface motion.

The ordinary kriging interpolation technique is very sensitive to the choice of the variogram model. It has to be chosen in such a way as to approximate the original semivariogram model of the interpolated data, which in turns depends on spatial distribution of sites (coordinates of the GPS stations) and its values (velocities). We found that Gaussian variogram model in horizontal directions and spherical variogram model in vertical direction [13] matches best our semivariograms.

Results of the kriging are presented on Fig. 1(a)–(c). The both horizontal components of velocity are smooth; the shortening effect is well observed in northeast direction perpendicular to the most strike-slip faults in the area as it was noticed in [7]. The vertical velocity is almost zero everywhere in the region with a few area of uplifts and subsidence with the velocity not larger than 1 cm/year.

D. GPS Errors

There are two sources of errors in the interpolated GPS data: those due to linear regression and those due to kriging. The error due to the linear regression can be easily estimated as a by-product of the regression analysis [14]. It mainly depends on the linearity of the time series. However, this error is known only at the sparse locations of the GPS sites.

The error due to kriging can be also estimated as a by-product of the kriging [9]. This error estimation is valid for each discretization point or pixel on the continuous GPS velocity

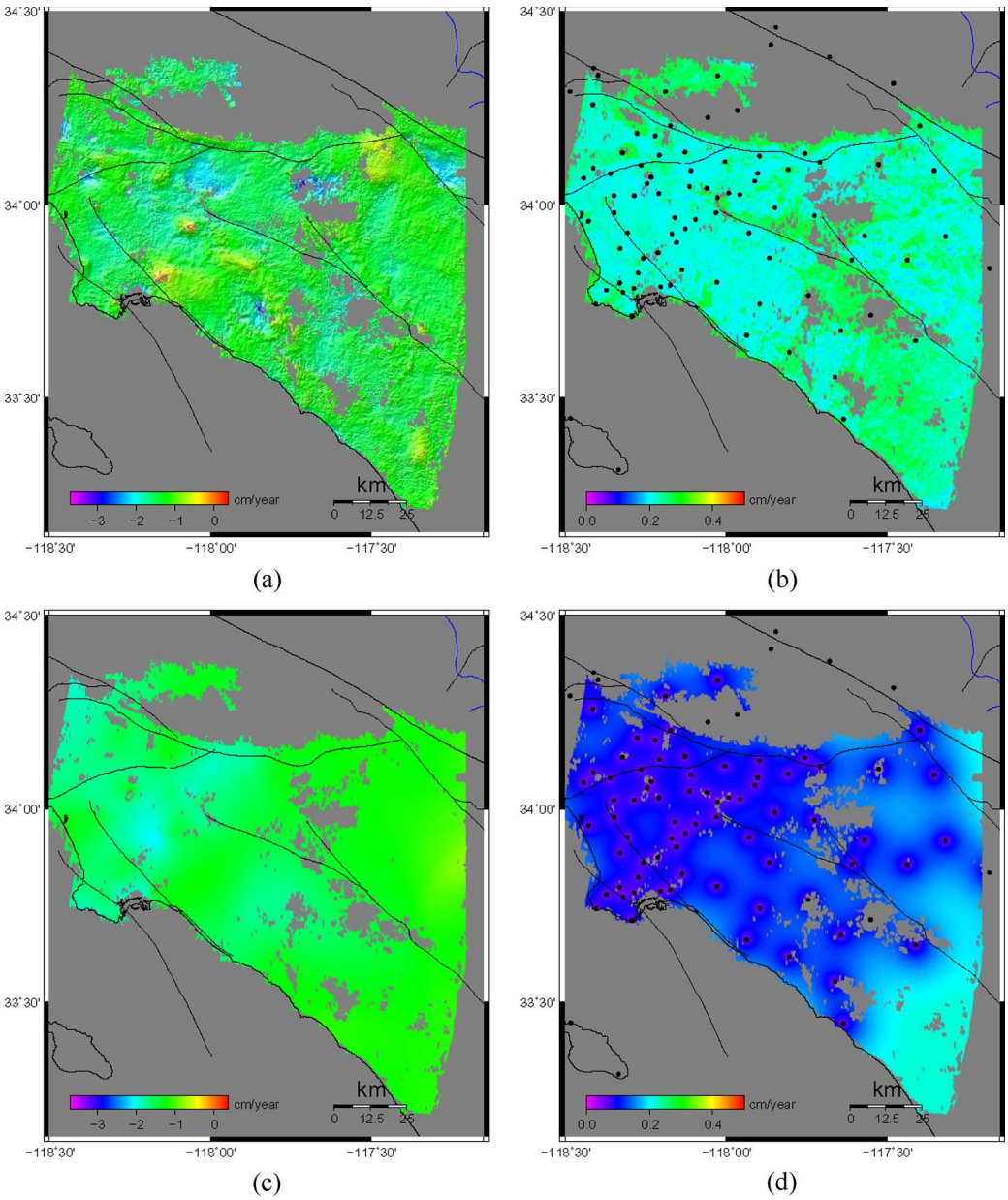

Fig. 2. Comparison of the ERS-2 differential interferogram with a time span of 2.97 years (September 2, 2000–August 23, 2003) and a perpendicular baseline $B_{\mathrm{p}} = 89$ m with the synthetic interferogram calculated from the interpolated GPS measurements. The total error of the DInSAR interferogram consists of the errors due to topography, decorrelation, atmospheric, and ionospheric noise. The total error of the synthetic interferogram was calculated according to the following equation: $\sigma^2_{V_{\mathrm{LOS}}} = S_x^2\sigma^2_{V_x} + S_y^2\sigma^2_{V_y} + S_z^2\sigma^2_{V_z}$. Both interferograms have the similar features and agree within the error. (a) ERS-2 000902-030823 DInSAR interferogram. (b) Standard deviation of DInSAR interferogram. (c) Interferogram calculated from GPS measurements. (d) Standard deviation of GPS interferogram.

map. It is equal to zero at the location of the GPS sites and increases with distance from the known position; therefore, reaching it maximum at the most remote areas.

In order to estimate the total GPS accuracy these two errors have to be combined, but in order to do this the error due to linear regression must be interpolated. We propose to do this by applying ordinary kriging interpolation again, but with the different (more suitable) variogram model. Then, these two errors can be combined by the following equation:

$$\sigma^2_{\mathrm{total}} = \sigma^2_{\mathrm{regression}} + \sigma^2_{\mathrm{kriging}}. \tag{13}$$

This method can be considered as the second approximation of the GPS error in comparison with the kriging error alone (the first approximation), as proposed in [5]. This total error is used as a weighting term in the final optimization equation.

The total errors of GPS velocities are presented in Fig. 1(d)–(f) for all three components. In general, the total errors are smaller at the GPS locations, especially when the GPS time series have a well-defined linear trend which then can be estimated by linear regression. A few GPS stations have large regression errors (for example in the southern part) which are due to the fact that the time series of those stations do not have a well-defined linear trend.

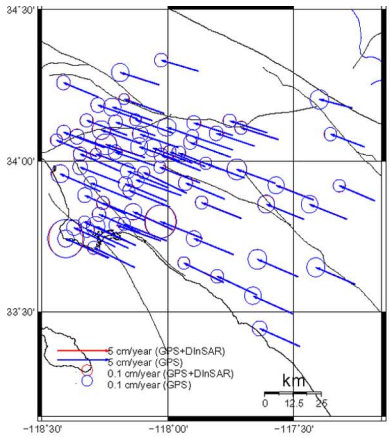

(a)

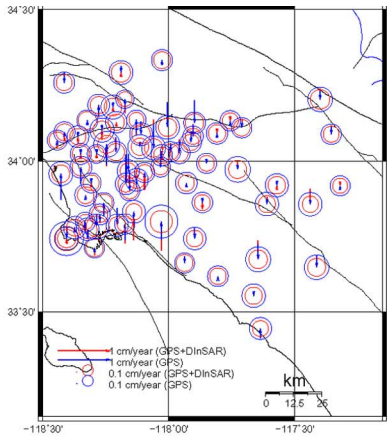

(b)

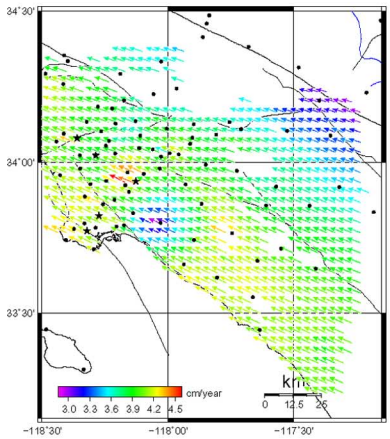

(c)

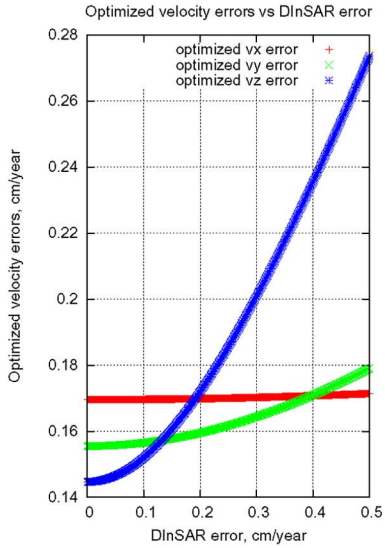

(d)

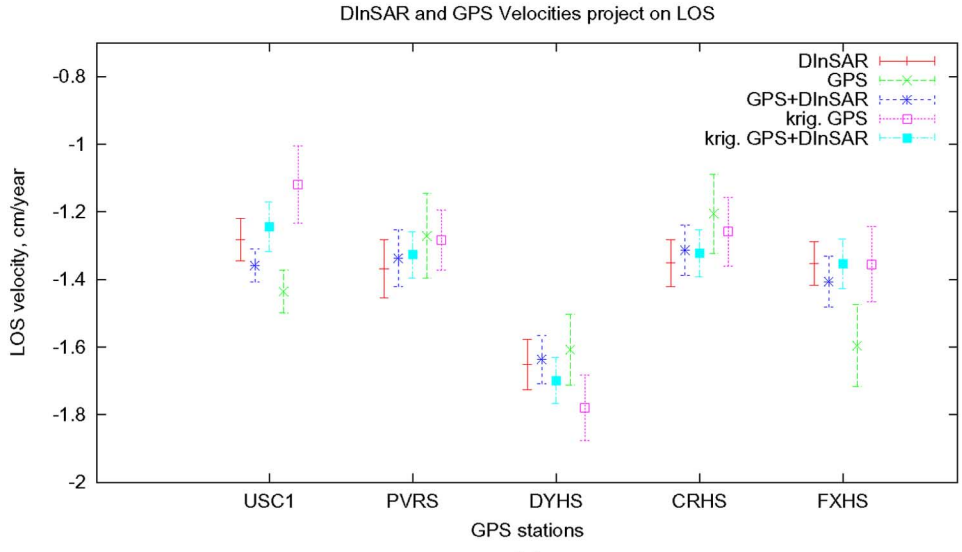

(e)

Fig. 3. Horizontal and vertical components of the velocities of the GPS sites with corresponding errors calculated from GPS measurements (blue) and optimized by using GPS + DInSAR data (red) and the complete horizontal velocity field of the region. (d) Shows the dependence of the components of the optimized velocities errors on the DInSAR error. The last plot (e) shows the results of cross validation test between projected on LOS GPS (marked as GPS) and DInSAR (marked as DInSAR) data. Also five GPS station [stars on Fig. 3(c)] were excluded from the modeling and the values at the same locations were calculated by the ordinary kriging interpolation (marked as krig. GPS). Then, optimization was performed for both sets with all GPS stations (marked as GPS + DInSAR) and without five GPS stations (marked as krig. GPS + DInSAR). (a) Horizontal component of the velocity. (b) Vertical component of the velocity. (c) Vector velocity map of the area. (d) Dependence of the optimized velocity errors on DInSAR error. (e) Cross validation of DInSAR and GPS range change rate.

E. DInSAR Data

In this paper, we used a DInSAR interferogram shown on Fig. 2(a) with a time span of 2.97 year (September 2, 2000–August 23, 2003). This interferogram was processed from ERS-2 level 0 (raw data) using the Jet Propulsion Laboratories (JPLs)/Caltech Repeat Orbit Interferometry Package (ROI_PAC, version 2.3) [15]. To reduce water vapor effects on the interferogram, the GPS/Moderate Resolution Imaging Spectroradiometer (MODIS) integrated water vapor correction model demonstrated in [16] was applied. This processing involved the usual steps of image coregistration, interferogram computation, baseline estimation from Delft precise orbits and interferogram flattening, and removal of topographic phase by using a 30-m shuttle radar topographic mission (SRTM) digital elevation model (DEM). At this stage, a zenith path delay difference map derived from GPS-calibrated MODIS near-infrared water vapor fields was inserted into the interferometric processing sequence, followed by phase unwrapping and baseline refinement. In order to obtain the unwrapped water-vapor-corrected interferogram, a new simulated interferogram was created using the refined baseline and topography, and was subtracted from the unwrapped phase (including orbital ramp) with the water vapor model removed [16].

Since interferometric synthetic aperture radar (InSAR) has no absolute reference datum, the unwrapped phase Fig. 2(c) has been shifted by the mean difference between InSAR and GPS range changes when compared to GPS-derived range changes in the LOS direction.

F. DInSAR Errors

Before the DInSAR interferogram can be used in this paper, all source of errors needs to be precisely estimated and corrected if possible. The error due to decorrelation was estimated as Cramer–Rao bound [17] for the phase standard deviation according to the following equation:

$$C_{\text{ins}} = \frac{1}{\sqrt{2N_l}} \frac{\sqrt{1-\gamma^2}}{\gamma} \tag{14}$$

where N_l is the number of looks, equal to 8 in our case and γ is the absolute value of correlation. The average value of error due to decorrelation was estimated to be approximately 0.23 cm/year.

This interferometric pair has a small baseline of 89 m, and the error in the SRTM DEM might lead to a phase error of up to 0.43 rad [16] or approximately 0.06 cm/year. This is assumed to be insignificant in comparison with other sources of error. The residual orbital tilts and offsets remaining in the interferogram were removed by subtracting a plane fitted to the unwrapped phase.

The atmospheric correction based on the GPS/MODIS integrated model was estimated and subtracted from the unwrapped interferogram. In order to validate the correction model, independent 3-D GPS-derived displacements were compared with InSAR results in the satellite LOS direction, which showed that the rms difference between GPS and InSAR decreased from 1.2 to 0.8 cm [16]. Assuming that both GPS and InSAR have the same accuracy, the error of the corrected InSAR range changes was estimated to be 0.19 cm/year $(0.8/\sqrt{2}/2.97 = 0.19)$ and constant for the entire interferogram in this paper.

TABLE I
DEPENDENCE OF THE OPTIMIZED VELOCITY ERROR MEASUREMENTS ON DInSAR ERROR CALCULATED FOR GPS SITE LOCATIONS ONLY (FIRST PART) AND THE WHOLE AREA (SECOND PART)

	v_{north} $cm/year$	v_{east} $cm/year$	v_{up} $cm/year$
GPS	0.14	0.14	0.21
GPS+DInSAR	0.14	0.13	0.16
Kriged GPS	0.17	0.16	0.25
Kriged GPS+DInSAR	0.17	0.15	0.18

Ionospheric errors were partially reduced by subtracting of the fitted plane from the unwrapped interferogram since they are usually long wavelength signals, linearly changing within interferograms [4].

The total error shown on Fig. 2(b) was calculated as the square root of the squared sum of all mentioned above errors and then used as the weighting parameter in the final optimization equation.

V. RESULTS

Once GPS and DInSAR data are selected and errors are calculated, the optimized velocity maps can be calculated by direct substitution into (8). Generally, this process is fast—it takes approximately 20 min to complete the calculation for the 100 × 100 km area on a 3-GHz Linux-based personal computer. The output of the calculations is the three components of the velocity vector. The process as presented here is completely automated; however, it can be altered at any time, for example, in order to remove systematic errors, eliminate noisy GPS stations, or remove incorrectly unwrapped patches of DInSAR interferogram.

A. Velocities at the GPS Locations

Fig. 3(a)–(b) presents the results for the calculations of horizontal and vertical components of the velocity vector calculated only at the GPS site locations. In this case, the kriging interpolation routine is not applied and, therefore, only the errors due to linear regression of the time series affect the GPS velocity calculations.

The improvement in accuracy is achieved for V_{east} and V_{up} components of the velocity. At the same time, the accuracy of V_{north} component does not change significantly. This dependence is expected, since the different components of the velocity vector contribute differently to the DInSAR interferogram. According to the following equation: $V_{\text{LOS}} = V_{\text{north}} S_{\text{north}} + V_{\text{east}} S_{\text{east}} + V_{\text{up}} S_{\text{up}}$, where S is the unit vector pointing from the point on the ground to the satellites (LOS direction). It

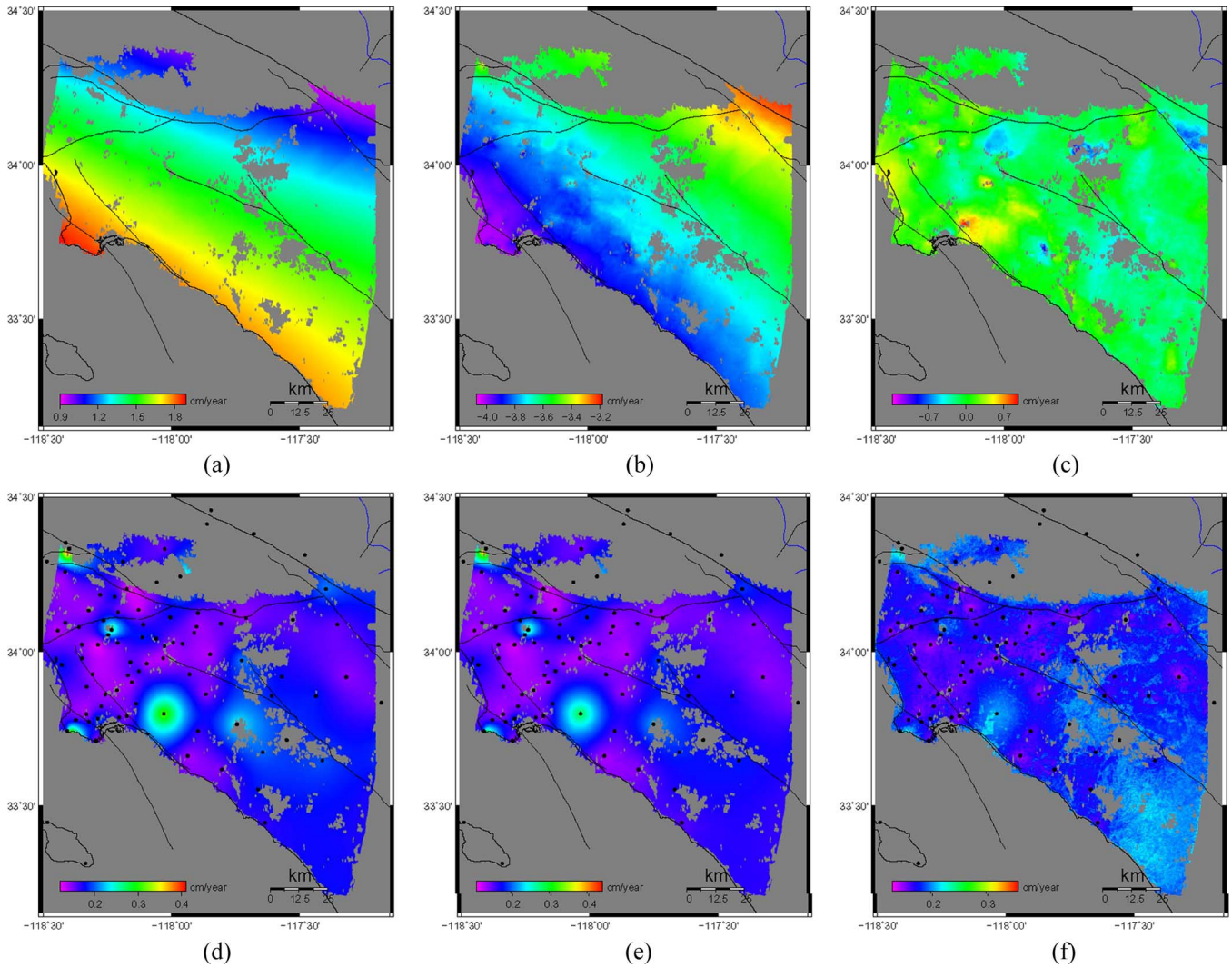

Fig. 4. Surface velocity field for the southern California region for the period between September 2, 2000 and August 23, 2003 with corresponding errors calculated from GPS and DInSAR measurements, obtained by minimizing the Gibbs energy function. (a) GPS + DInSAR optimized V_{north} component of velocity. (b) GPS + DInSAR optimized V_{east} component of velocity. (c) GPS + DInSAR optimized V_{up} component of velocity. (d) Standard deviation of V_{north}. (e) Standard deviation of V_{east}. (f) Standard deviation of V_{up}.

has the following components $\{-0.08,\ 0.30,\ 0.95\}$. These values slightly change within the interferogram. Therefore, the contribution of the north component of the velocity to the interferogram practically negligible. At the same time, the contribution of the vertical component is quite significant, and the contribution of the east component is moderate. It is worth mentioning that the S_{up} factor is almost the same across the scene. This is because the incidence angle of ERS-1/2 varies with the limited range of $(19.35^{\circ}-26.50^{\circ})$ and a mean of 23° [18]. The contribution of each of the horizontal components will vary depending on the satellite orientation in the chosen coordinate system.

The first part of the Table I shows the average error for each component of the velocity before and after optimization. Note that, the improvement in accuracy for each particular point on the ground will vary: it will be larger in cases where the original error of the velocity is large and smaller where the original error is small. The magnitude of the improvement depends on the DInSAR error at that point in the way presented in the Fig. 3(d). This figure shows the dependence of the errors of each component of the optimized velocities on the DInSAR error.

B. Derivation of Continuous Velocity Maps

In this case, ordinary kriging is used in order to interpolate GPS data at the intermediate locations. After that the optimized velocities are calculated by the direct substitution into (8). The optimization results are presented in Fig. 4(a)–(c) and the errors, calculated by (11) are presented on Fig. 4(d)–(f). As for the GPS sites alone, the improvement of accuracy is largest for the vertical V_{up} component and moderate for the V_{east} component. This error is analysis presented in the second part of Table I.

The appearance of the northern image practically does not change due to the orientation of the satellite in the current coordinate system, as explained above. The eastern component of the velocity, however, has more significant changes, especially in the southern part. The strong velocity gradient in both north

and east components is noticeable, which suggests that this analysis can be used to improve the accuracy of the estimation of shortening across the Los Angeles basin.

The vertical component shows the combination of signals from both GPS and DInSAR measurements. A few areas are of particular interest. A strong uplift with the approximate velocity of 06–0.8 cm/year is observed in the southern part of the Los Angeles basin (34.8 N, −118.2 E), due to seasonal changes in the groundwater levels. These results are in good agreement with those in [16] and [7]. A few areas of subsidence are presented in the northern part of the image. The middle region (around 34 N, −117.6 E) is the rapid subsidence which is presented on many other interferograms starting from approximately the mid-1990s [7]. The top right subsidence (34.1 N, −117.2 E) that is originally presented only on the DInSAR interferogram is amplified on the final image and contours the fault.

All three components of the error maps have similar patterns but differ in magnitude. The smallest error, present in the middle of the image where dense GPS coverage is achieved, suggests that the error due to kriging is minimal. The southeast corner has very sparse GPS coverage and, therefore, larger errors.

The vector map of the horizontal motion of combined north and east components is presented on the Fig. 3(c).

In order to assess the possible uncertainty introduced by the ordinary kriging interpolation, comparisons between interpolated and measured values were performed in the LOS direction. Five randomly picked GPS sites (USC1, DYHS, FXHS, CRHS, PVRS) from the spatially densest part of the region [stars in Fig. 3(c)] were excluded in the interpolation processes and were used later as a validation network. The results of this test are presented in Fig. 3(e). It is clear that the interpolated velocities (marked as krig. GPS) of four out of five GPS stations (except USC1) agree well with those measured values (marked as GPS) (i.e., within 1 sigma). Also, there is no systematic error (bias) observed among GPS, krig. GPS, and DInSAR values. In the GPS + DInSAR optimized case, the interpolated (marked as krig. GPS + DInSAR) and measured (marked as GPS + DInSAR) values are consistent with each other (i.e., within 1 sigma) for all the five stations. This means that this technique is not sensitive to the number of GPS stations, at least when the velocity field is smooth.

VI. Summary and Conclusion

We present here a method to derive continuous velocity maps of the southern California region from spatially sparse temporally dense GPS measurements and spatially dense temporally sparse DInSAR interferograms. It is shown that this technique can be used to improve the accuracy of the current GPS velocities, and also to derive a continuous 3-D surface velocity field with a high degree of accuracy.

The significance of this method is that it allows for the statistically coherent combination of both GPS and DInSAR data in an unambiguous way and at the same time to account for the errors due to the measurements of both data sets.

The accuracy of the calculations can be significantly improved if two (for example, ascending and descending) or more interferograms are available and used for the optimization. Also, there is the potential to include additional data sets to this method, such as leveling data, lidar, or the SAR data from different satellites. In addition, even GPS velocities with small measurement errors potentially can be improved if a stacked interferogram over a longer time span is used, instead of a single DInSAR image. At the same time, in regions with high vegetations where a DInSAR interferogram decorrelates quickly, the new permanent scatters method can be incorporated into the analysis.

Acknowledgment

The work of Z. Li was performed at University College London as part of the activities of the Natural Environment Research Council Earth Observation Centre of Excellence: Centre for the Observation and Modelling of Earthquakes and Tectonics. The ERS data were supplied under European Space Agency environmental satellite data Grant AO ID = 853 (HAZARDMAP). Technical support for this work has been provided by the POLARIS network. The DInSAR data was processed by the Repeat Orbit Interferometry Package (ROI_PAC) developed at Caltech/JPL. The DEM data was provided by United States Geological Survey. The GPS data was downloaded from SCIGN web site. The images were plotted with the help of GMT software developed and supported by P. Wessel and W. H. F. Smith.

References

[1] S. Samsonov and K. Tiampo, "Analytical optimization of DInSAR and GPS dataset for derivation of three-dimensional surface motion," *IEEE Geosci. Remote Sens. Lett.*, vol. 3, no. 1, pp. 107–111, Jan. 2006.

[2] T. Tsuda, K. Heki, S. Miyazaki, K. Aonashi, K. Hirahara, H. Nakamura, M. Tobita, F. Kimata, T. Tabei, T. Matsushima, F. Kimura, M. Satomura, T. Kato, and I. Naito, *GPS Meteorology Project of Japan—Exploring Frontiers of Geodesy, Earth Planets Space*, vol. 50, no. 10, i–v, 1998.

[3] K. W. Hudnut, Y. Bock, J. E. Galetzka, F. H. Webb, and W. H. Young, "The southern California integrated GPS network (SCIGN)," in *Proc. Int. Workshop Seismotectonics Subduction Zone*, Y. Fujinawa, Ed., Tsukuba, Japan, 1999, pp. 175–196.

[4] D. Massonnet and K. Feigl, "Radar interferometry and its application to changes in the Earth surface," *Rev. Geophys.*, vol. 36, no. 4, pp. 441–500, 1998.

[5] S. Gudmundsson, F. Sigmundsson, and J. Carstensen, "Three-dimensional surface motion maps estimated from combined interferometric synthetic aperture radar and GPS data," *J. Geophys. Res.*, vol. 107, no. B10, pp. ETG13.1–ETG13.14, 2002.

[6] D. Dong, T. Herring, and R. King, "Estimating regional deformation from a combination of space and terrestrial geodetic data," *J. Geod.*, vol. 72, no. 4, pp. 200–214, Apr. 1998.

[7] K. Watson, Y. Bock, and D. Sandwell, "Satellite interferometric observation of displacements associated with seasonal groundwater in Los Angeles Basin," *J. Geophys. Res.*, vol. 107, no. B4, pp. ETG8-1–ETG8-12, 2002.

[8] P. Brooker, *A Geostatistical Primer*. Singapore: World Scientific, 1991.

[9] C. Deutsch and A. Journel, *GSLIB Geostatistical Software Library and User's Guide*. London, U.K.: Oxford Univ. Press, 1992.

[10] J. Taylor, *An Introduction to Error Analysis: The Study of Uncertanties in Physical Measurements*. Herndon, VA: Univ. Sci. Books, 1982.

[11] A. Ferreti, C. Prati, and F. Rocca, "Permanent scatterers in SAR interferometry," *IEEE Trans. Geosci. Remote Sens.*, vol. 39, no. 1, pp. 8–20, Jan. 2001.

[12] G. Bawden, W. Thatcher, R. Stein, K. Hudnut, and G. Peltzer, "Tectonic contraction across Los Angeles after removal of groundwater pumping effects," *Nature*, vol. 412, no. 6849, pp. 812–815, 2001.

[13] E. J. Pebesma and C. G. Wesseling, "Gstat: A program for geostatistical modelling, prediction and simulation," *Comput. Geosci.*, vol. 24, no. 1, pp. 17–31, 1998.
[14] W. Press, S. Teukolsky, W. Vetterling, and B. Flannery, *Numerical Recipes in C: The Art of Scientific Computing*. Cambridge, U.K.: Cambridge Univ. Press, 1992.
[15] P. Rosen, S. Hensley, G. Peltzer, and M. Simons, "Updated repeat orbit interferometry package released," *EOS, Trans. AGU*, vol. 85, no. 5, p. 47, 2004.
[16] Z. Li, J.-P. Muller, P. Cross, and E. J. Fielding, "Interferometric synthetic aperture radar (InSAR) atmospheric correction: GPS, Moderate Resolution Imaging Spectroradiometer (MODIS), and InSAR integration," *J. Geophys. Res.*, vol. 110, no. B3, B03410, 2005.
[17] E. Rodriguez and J. Martin, "Theory and design of interferometric synthetic aperture radars," *Proc. Inst. Elect. Eng. F, Radar Signal Process.*, vol. 139, no. 2, pp. 147–159, Apr. 1992.
[18] C. Olmstead, *Scientific SAR User's Guide*. Fairbanks, AK: Alaska SAR Facility, 1993.

Sergey Samsonov received the B.S. and M.S. degrees in physics from Moscow State University, Moscow, Russia, in 1999. He is currently working toward the Ph.D. degree in geophysics and environmental science at the University of Western Ontario, London, ON, Canada.

His field of research is focused on geophysics, remote sensing and integration of interferometric synthetic aperture radar, and GPS measurements for the study of surface deformation.

Kristy Tiampo received the B.S.C.E. degree from Tufts University, Medford, MA, in 1983, the M.S. degree from Stanford University, Stanford, CA, in 1984, and the Ph.D. degree from the University of Colorado, Boulder, in 2000.

She is currently an Assistant Professor of geophysics specializing in seismicity and geodesy with the Department of Earth Sciences, University of Western Ontario, London, ON, Canada. Her research is focused on understanding the underlying physics of the earthquake system through advanced data analysis techniques in geodesy and seismology, the pattern analysis of fault systems, and data assimilation into computational simulations of the fault network.

Dr. Tiampo is a member of Tau Beta Pi.

John Rundle received the B.S.E. degree from Princeton University, Princeton, NJ, in 1972, and the M.S. and Ph.D. degrees from the University of California, Los Angeles, in 1973 and 1976, respectively.

He is currently the Director of the Computational Science and Engineering Center, University of California, Davis. His research is focused on understanding the dynamics of earthquakes through numerical simulations, pattern analysis of complex systems, dynamics of driven nonlinear earth systems, and adaptation in general complex systems.

Dr. Rundle received the Distinguished Visiting Scientist at the Jet Propulsion Laboratory in Pasadena, CA; Aki award for distinguished service as Chair of the Advisory Council of the Southern California Earthquake Center, in 1994–1996; chosen as Lorenz Lecturer at the December 2004 American Geophysical Union meeting in San Francisco; and election as a Fellow of the American Physical Society, in 2005. He is also a member of Phi Beta Kappa and Tau Beta Pi.

Zhenhong Li was born in China, in 1975. He received the B.Sc. degree (first-class honors) in geodesy from Wuhan Technical University of Surveying and Mapping (now Wuhan University), Wuhan, China, in 1997, and the Ph.D. degree in geodesy and navigation from University College London, London, U.K., in 2005.

His main research interest is the use of InSAR, GPS, and other space-based techniques for monitoring surface deformation, and he specializes in InSAR atmospheric water vapor correction models. To date, he has developed five water vapor correction models to reduce water vapor effects on InSAR measurements using GPS, Moderate Resolution Imaging Spectroradiometer, and Medium Resolution Imaging Spectrometer data. He is currently working on detection of slow deformation rates using water vapor correction models in combination with phase stacking and/or time-series techniques.

Dr. Li won a Student Paper Prize and a Best Paper Presentation Award at the Institute of Navigation Satellite Division Technical Meeting (ION GNSS) conference in 2004, and was awarded a travel grant by the International Association of Geodesy (IAG) for the IAG Scientific Assembly in 2001.